INTERNATIONAL SOCIETY FOR
SOIL MECHANICS AND
GEOTECHNICAL ENGINEERING

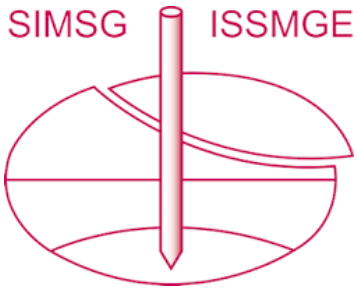

This paper was downloaded from the Online Library of the International Society for Soil Mechanics and Geotechnical Engineering (ISSMGE). The library is available here:

https://www.issmge.org/publications/online-library

This is an open-access database that archives thousands of papers published under the Auspices of the ISSMGE and maintained by the Innovation and Development Committee of ISSMGE.

The paper was published in the Proceedings of the 8th International Symposium on Deformation Characteristics of Geomaterials (IS-PORTO 2023) and was edited by António Viana da Fonseca and Cristiana Ferreira. The symposium was held from the 3rd to the 6th of September 2023 in Porto, Portugal.

IS-PORTO 2023 PROCEEDINGS

Proceedings of the 8th International Symposium on DEFORMATION CHARACTERISTICS OF GEOMATERIALS Porto, 3rd - 6th September 2023

Investigation of diatomaceous sand using elastic and electromagnetic waves in oedometer tests

Ngoc Quy Hoang[1], *Sang Yeob* Kim[2], *Dongsoo* Lee[1], and *Jong-Sub* Lee[1#]

[1]*School of Civil, Environmental and Architectural Engineering, Korea University, 145, Anam-ro, Seongbuk-gu, Seoul, 02841, Korea*

[2]*Department of Fire and Disaster Prevention, Konkuk University, 268 Chungwon-daero, Chungju, 27478, Korea*

[#]*Corresponding author: jongsub@korea.ac.kr*

ABSTRACT

The small-strain and electromagnetic behaviors of soils significantly change due to compression. The objective of this study was to investigate the small-strain stiffness and electrical resistivity of diatomaceous sand by modifying the conventional setup of oedometer tests (1D-compression tests). The specimens used were pure sand and sand with 20% diatoms by weight. The vertical displacement was directly observed using a digital gauge at the top of the compression cap during compression. At the end of each loading step, shear waves (S-waves) are measured using a pair of bender elements installed on the top and bottom compression caps. In addition, electrical resistance was measured using a pair of electrodes installed horizontally in the middle of the compression cylinder. The test results show that the compression index increased but the swelling index decreased according with the increase in the amount of the small and crushable diatom particles. The presence of diatom particles weakened the interparticle contacts and softened the soil skeletons. In addition, the electrical resistivity increased with the increase in diatom contents, which increased the surface conduction. Our work suggests that the S-wave velocity and electrical resistivity of diatomaceous sand can be characterized by modifying the conventional oedometer tests.

Keywords: Diatom; Electrical resistivity; Oedometer; S-wave.

1. Introduction

Diatoms are commonly found in marine sediments in deep seabeds such as Osaka Bay (Japan) and Ulleung Basin (Korea) (Shiwakoti et al., 2002; Lee et al., 2011, 2013). Diatoms grow in sunlit water areas that are rich in silica and consume silica to build their skeleton (Tréguer et al., 1995). Diatom dead bodies settle on sea floors and dissolve the silica forming new deposits (Díaz-Rodríguez et al., 1998; Tanaka & Locat, 1999; Owen et al., 2010; Caicedo et al., 2018). The presence of diatoms affects the engineering properties and behavior of marine sediments (Tanaka & Locat, 1999; Shiwakoti et al., 2002; Hong et al., 2006; Wiemer et al., 2017). In addition, small and soft diatom particles in soil skeleton form weak interparticle contacts and increase the attenuation of shear waves (Assefa et al., 1999), which significantly affects the soil stiffness. With high intra-porosity (Burger & Shackelford, 2001) and high specific surface (Zhang et al., 2011), the diatom may govern the electrical resistivity of soils. Hence, this study was conducted to investigate the small-strain and electrical resistivity behaviors of diatomaceous soil. Two specimens, including pure sand and a sand-diatom mixture, were used in the oedometer tests. The vertical displacement was observed using a digital gauge. In addition, the oedometer apparatus was modified to attach a pair of bender elements and a pair of electrodes for shear wave and electrical resistance measurements at every loading step.

2. Experimental setup

2.1. Specimens

Table 1. Oedometer test specimens

Specimen	Sand content (%)	Diatom content (%)	Density (g/cm^3)
DC00 (sand)	100	0	1.398
DC20	80	20	1.398

Two artificial specimens, named DC00 and DC20, were used in this study, as listed in Table 1. Their grain size distributions (GSD) are plotted in Fig. 1. DC00 was the specimen of uniformly graded sand with a density of

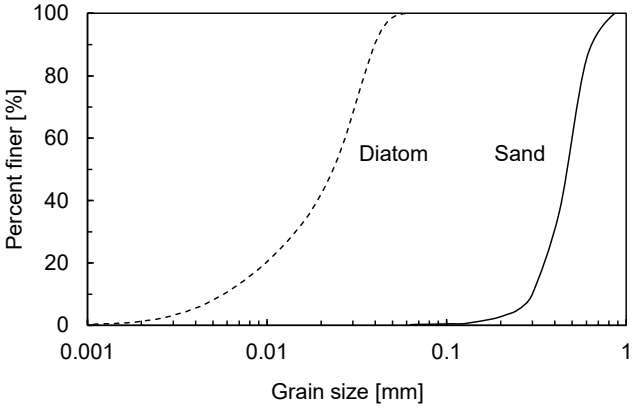

Figure 1. Grain size distribution of sand and diatom

1.398 g/cm^3 (relative density of 80%), a medium size (D50) of 0.47 mm, and a specific gravity of 2.65, as summarized in Table 1. The sand particles are sub-rounded, as shown in Fig. 2 (a). DC20 is the specimen formed by replacing 20% of the amount of sand (by dry weight) in DC00 with diatoms. Thus, the density of DC20 remains equal to that of DC00, i.e., 1.398 g/cm^3.

(a)

(b)

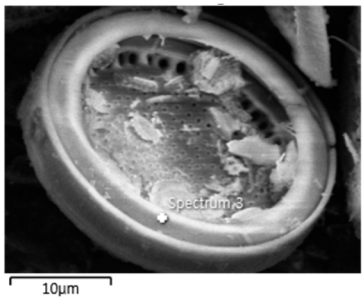

Figure 2. Sand and diatom: (a) sand particles; (b) diatom particles

The diatoms used in this study were Coscinodiscus disc-like frustules as shown in Fig. 2 (b). The diatom was uniformly graded with a D50 of 22 μm and a specific gravity of 2.2, as shown in Fig. 1. The two specimens were placed well into an oedometer cell with a height of 70 mm and diameter of 58 mm and saturated with tap water.

2.2. Oedometer tests

For deformation characterization, standard oedometer tests, including a loading phase (5 kPa to 1280 kPa) and an unloading phase (1280 kPa to 5 kPa), were conducted for the DC00 and DC20 specimens. The specimens were saturated with tap water before the oedometer tests, and the saturation condition was sustained by maintaining the water level above the specimen, as shown in Fig. 3. The vertical compression loads were applied to the top cap of the odometer cell using a metal rod and measured using a load cell connected to a data logger. Oedometer tests include loading tests from 5 to 1280 kPa and unloading tests from 1280 to 5 kPa. Each loading or unloading step proceeded after verifying the completion of the previous step using the graph of vertical displacement vs time.

The vertical displacement was directly observed by a digital gauge at the top of the specimens and recorded by the connected data logger, as shown in Fig. 3.

2.3. Measurement systems

For the small-strain and electrical resistivity characterization, a measurement system was adopted, as shown in Fig. 3. Fig. 3 shows that the shear wave (S-wave) was measured via a pair of bender elements installed on the top and bottom caps (Lee & Santamarina, 2005). The benders were placed in a plastic house and shielded with epoxy to eliminate electrical noise and frame waves (Lee & Santamarina, 2005; 2006). A single sinusoidal signal was generated using the top bender element, and the propagated waves were detected by the bottom bender element. The signals were filtered and amplified by a filter/amplifier, and captured by an oscilloscope, as shown in Fig. 3.

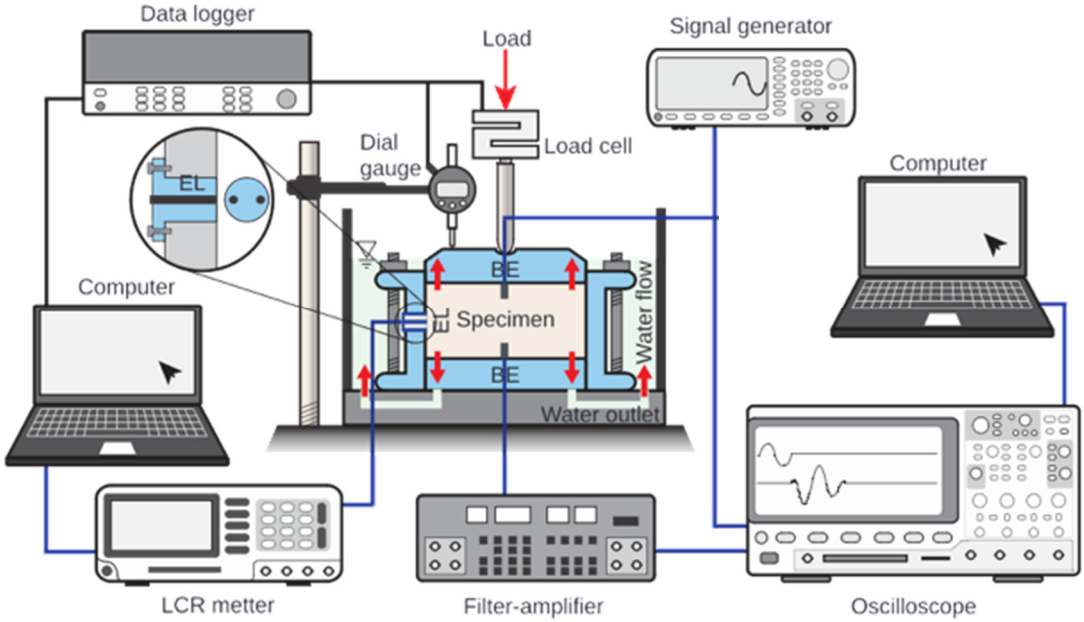

Figure 3. Schematic diagram of the oedometer test setup. BE: bender elements; EL: electrodes; LCR: inductance-capacitance-resistance

Electrical resistance was measured using a pair of electrodes installed horizontally in the middle of the compression cylinder. The electrodes were placed in a plastic house and shielded with epoxy resin to eliminate electrical noise. Finally, the electrodes were connected to an LCR meter, and the data were stored in a computer linked. Electrical resistance was converted to electrical resistivity using a linear calibration performed on water with different salinities (Cho et al., 2004), as shown in Fig. 4. Fig. 4 shows that the relationship between the electrical resistance and electrical resistivity is linear, with a coefficient of determination (R) of 0.9999.

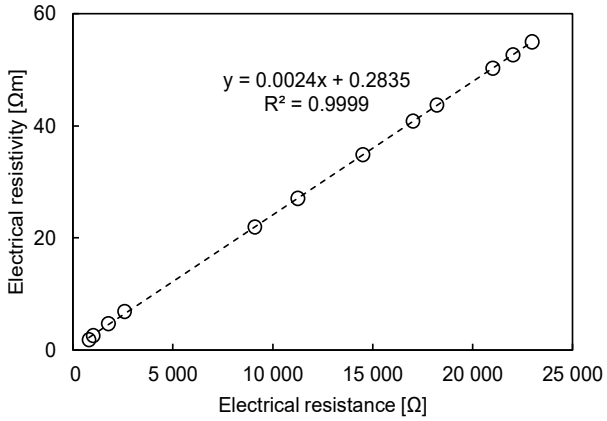

Figure 4. Electrical resistivity calibration

The S-wave and electrical resistance were alternately measured at the end of each loading step.

3. Experimental results

3.1. Displacement

The displacements of the two specimens during loading and unloading were observed and used to calculate the void ratios. The results were summarized and plotted in Fig. 5. Fig. 5 shows that for DC00, the void ratio decreased significantly as the vertical effective stress increased. For instance, the void ratio value of 0.61 at 640 kPa was decreased to approximately 0.49 at 1280 kPa. During unloading, the void ratio increased as the vertical effective stress increased. The difference between the loading and unloading indicates plastic deformation, which is not recoverable.

DC20 showed a similar trend: the void ratio slightly decreased in the first few steps and significantly decreased at 640 and 1280 kPa. However, DC00 exhibited lower void ratios than DC20. The loading curve for DC20 is steeper than that for DC00. However, the unloading curve of DC00 is steeper than that of DC20.

3.2. Shear wave

The S-wave signals were captured during the oedometer tests, and the S-wave velocity was calculated using the first arrivals and travel distances, which is the tip-to-tip distance between the two bender elements, as shown in Fig. 3. Fig. 6 shows the S-wave velocity for the

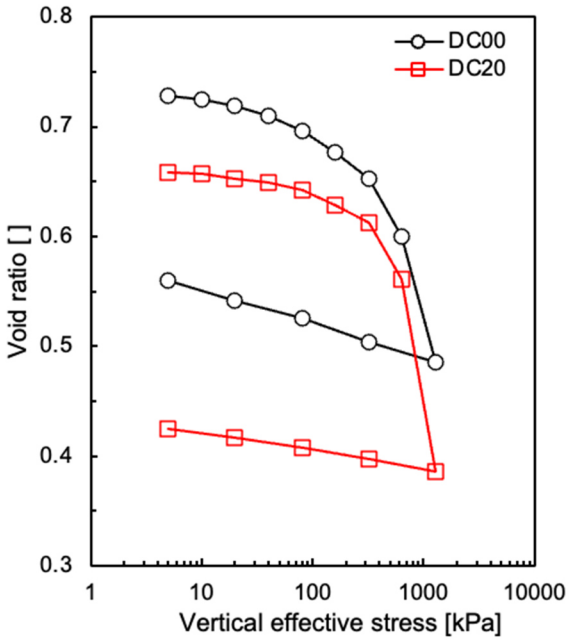

Figure 5. Void ratio vs vertical effective stress

loading steps versus the vertical effective stress. For DC00, the S-wave velocity increased from 141 m/s to 407 m/s as the vertical effective stress increased from 5 to 1280 kPa. Similarly, for DC20, the S-wave velocity increased from 80 m/s (at 5 kPa) to 226 m/s (at 1280 kPa). The S-wave velocities of DC00 were higher than those of DC20.

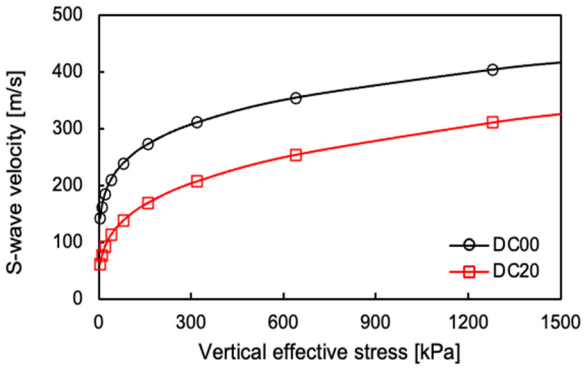

Figure 6. S-wave velocity vs vertical effective

3.3. Electrical resistivity

The electrical resistance was directly measured at every loading step using the measurement system (Fig. 3) and calibrated to the electrical resistivity using the linear equation, as shown in Fig. 4. The electrical resistivity values were summarized and plotted in Fig. 7. Fig. 7 shows that for DC00, the electrical resistivity increased from 257 to 304 Ωm as the vertical effective stress increased from 5 to 640 kPa and significantly increased to 373 Ωm at 1280 kPa. DC20 showed a similar trend to DC00 but lower electrical resistivity values compared to those of DC00. For DC20, the electrical resistivity increased from 189 Ωm at 5 kPa to 222 Ωm at 640 kPa, and significantly increased to 322 Ωm at 1280 kPa.

4. Analysis and discussion

4.1. Compressibility

The compression and swelling indices for DC00 and DC20 were calculated using Fig. 5 and plotted in Fig. 8. Fig. 8 shows that the compression index increased from

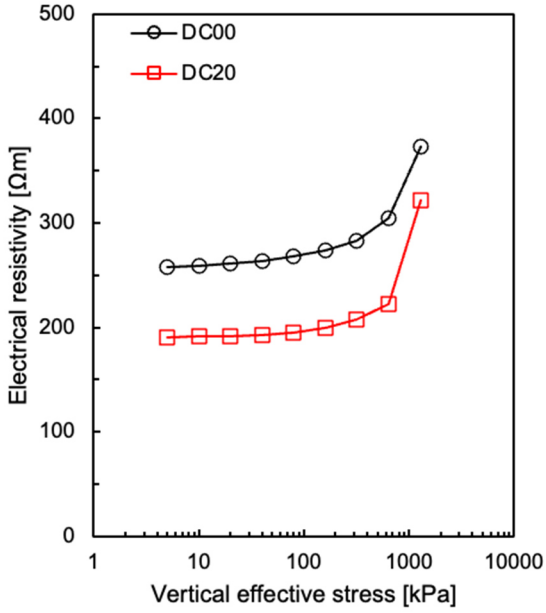

Figure 7. Electrical resistivity vs vertical effective stress

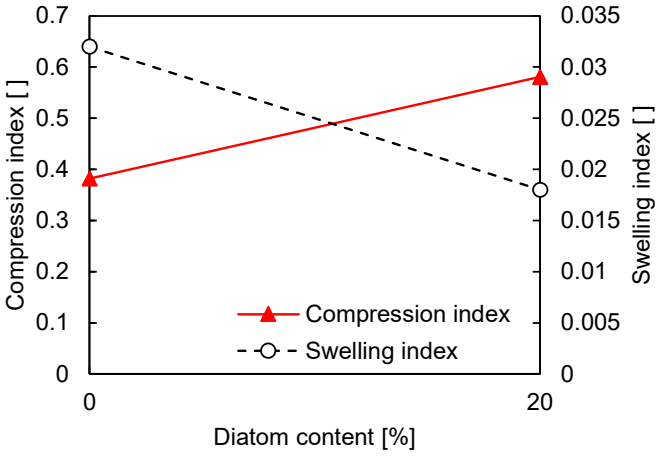

Figure 8. Compression and swelling indices

0.38 (DC00) to 0.58 (DC20) when diatoms were added. The increase in the compression index can be attributed to the high intra-porosity of the diatoms (Tanaka & Locat, 1999; Shiwakoti et al., 2002). Thus, the density of DC20 was equal to that of DC00, but the void ratio of DC20 was lower than that of DC00. The added diatoms filled the pores among the sand particles (inter-porosity) and decreased the inter-porosity. However, diatom particles are excessively porous because of the small pores with diameters ranging from 30 to 1000 nm crushable (Losic et al., 2007; Zhang et al., 2011) which increase the intra-porosity of the soil. The soil becomes more compressible, and the compression index increases.

The swelling index decreased from 0.032 (DC00) to 0.018 (DC20). The swelling index indicates the elastic deformation of a material. The decrease in the swelling index might be caused by the rearrangement of sand and diatom particles, which is irreversible during unloading. In addition, the diatoms may be crushed into small pieces during loading and cannot recover their original shape during unloading (Hong et al., 2006; Wiemer et al., 2017). Thus, the swelling index decreased.

For comparison between DC00 and DC20, the vertical strains of DC00 and DC20 were calculated using Fig. 5 and plotted in Fig. 9. Fig. 9 shows that DC20 displaced much more than DC00 during loading but did not swell as much as DC00 did during unloading. The plastic deformation, i.e., the gap between loading and unloading in Fig. 9, increases because of the presence of the diatom, and it is an indication of the diatom crushing phenomenon.

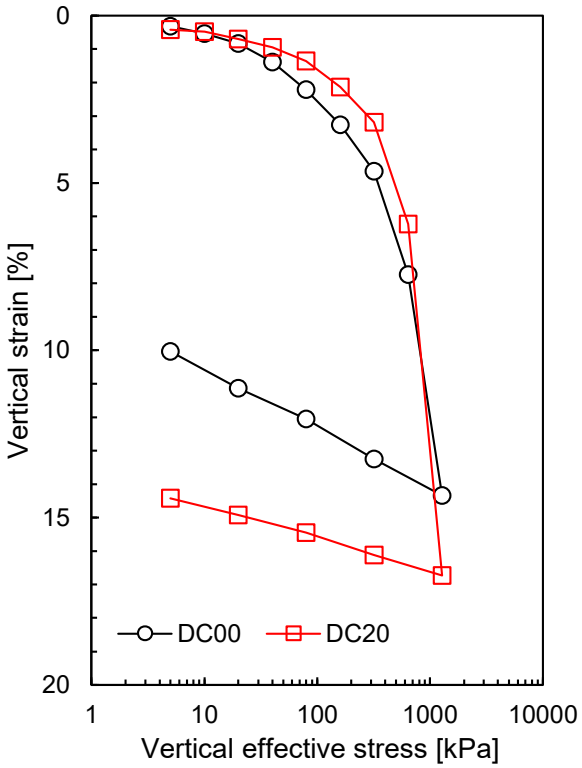

Figure 9. Vertical strain

4.2. Deterioration of soil skeleton

The decrease in S-wave velocity indicates the deterioration of the soil skeleton (Salgado et al., 2000; Carraro et al., 2009). The diatom used in this study had very high intra-porosity (porosity of its particle) with pores ranging from 30 to 1000 nm and was very crushable (Losic et al., 2007; Zhang et al., 2011). This diatom is porous and soft compared to sand particles. For DC20, 20% diatoms were added to replace the same amount of sand. Porous and soft diatom particles in the soil, therefore, soften the soil skeleton and the interparticle contacts.

For the analysis of S-wave, the S-wave velocity can be expressed as follows:

$$V_s = \alpha \left(\frac{\sigma'_p + \sigma'_m}{2kPa} \right)^{\beta} \quad (1)$$

where V_s is the S-wave velocity; σ'_p and σ'_m are the effective stresses acting in the wave propagation direction and the particle motion direction, respectively; $\sigma'_m = (1 - sin\phi)\sigma'_v$; the friction angle $\phi = 40.0^o$ for DC00 and $\phi = 26.1^o$ for DC20; α is the factor of S-wave velocity at 1 kPa; and β is the exponent factor. It is to be noted that values of β increase from $\beta \approx 0$ for cemented soils (Fernandez & Santamarina, 2001; Yun & Santamarina, 2005), and to $\beta \approx 0.7$ for soft and weak particle soils (Lee et al., 2007; Cha et al., 2014). The estimations of α and β are shown in Table 2 as follows:

Table 2. α and β factors.

Specimen	α (m/s)	β ( )
DC00 (sand)	112.4	0.189
DC20	41.7	0.291

Table 2 shows that β increased from 0.189 to 0.291 as the diatom content increases. The increase in β indicates the deterioration in inter-particle contact and soil skeleton (Santamarina et al., 2001).

4.3. Development of surface conduction

The electrical resistivity of soils can be defined as follows:

$$\sigma_{soil} = n\sigma_{el} + (1 - n)\frac{\gamma_p}{g}S \quad (2)$$

where $\sigma_{soil}, \sigma_{el}$ are the electrical conductivities of the soil and electrolyte, respectively; n is the porosity; γ_p is the unit weight; g is the gravitational constant; λ_{ddl} is the electrical conductivity at the surface; and S is the total surface conduction. The unit weight and electrolyte conductivity were equal for DC00 and DC20. Thus, the porosity and total surface conduction govern the soil's electrical resistivity of the soil. The experimental results showed that the electrical resistivity decreased after adding diatoms. The diatoms with a specific surface of 27·86 m^2/g (Zhang et al., 2011) may significantly increase the surface conduction of the soils, thus decreasing the electrical resistivity of DC20. Note that the electrical resistivity is the inverse of electrical conduction.

5. Summary and conclusion

This study aims to characterize the small-strain shear stiffness and electrical resistivity of diatomaceous sand. Oedometer tests were conducted on specimens of pure sand (DC00) and a mixture of sand and 20% diatoms (by weight). The oedometer test consisted of two phases: loading from 5 to 1280 kPa and unloading from 1280 to 5 kPa. The vertical displacement, S-wave, and electrical resistance were measured. From the experimental results, the following observations were made:

- The compression index increased, but the swelling index decreased as small and crushable diatom particles broke into small pieces, which could not recover.
- The soil skeleton was softened in the sand with diatom, and interparticle contacts were weakened due to the soft and crushable diatom particles.
- The electrical resistivity decreased as the diatom content increased, which is an indication of increase in the surface conduction of the soil with the addition of diatoms.

Acknowledgements

This research was supported by the Basic Science Research Program through the National Research Foundation of Korea (NRF) funded by the Ministry of Science, ICT and Future Planning (NRF-2021R1A5A1032433).

References

Assefa, S., McCann, C. & Sothcott, J. (1999). Attenuation of P - and S-waves in limestones. Geophys. Prospect. 47, No.3, 359–392. https://doi.org/10.1046/j.1365-2478.1999.00136.x

Burger, C. A. & Shackelford, C. D. (2001). Evaluating dual po rosity of pelletized diatomaceous earth using bimodal soil-water characteristic curve functions. Can. Geotech. J. 38, N o. 1, 53–66. https://doi.org/10.1139/t00-084

Caicedo, B., Mendoza, C., López, F. and Lizcano, A. (2018). B ehavior of diatomaceous soil in lacustrine deposits of Bogo tá, Colombia. J. Rock Mech. Geotech. Engng 10, No. 2, 36 7–379. https://doi.org/10.1016/j.jrmge.2017.10.005

Carraro, J. A. H., Prezzi, M. and Salgado, R. (2009). Shear stre ngth and stiffness of sands containing plastic or nonplastic fines. J. Geotech. Geoenviron. Engng 135, No. 9, 1167–11 78. https://doi.org/10.1061/(asce)1090-0241(2009)135:9(1167)

Cha, M., Santamarina, J. C., Kim, H. S. and Cho, G. C. (2014) . Small-strain stiffness, shear-wave velocity, and soil comp ressibility. J. Geotech. Geoenviron. Engng 140, No. 10, 06 014011. https://doi.org/10.1061/(asce)gt.1943-5606.0001157

Cho, G. C., Lee, J. S. and Santamarina, J. C. (2004). Spatial va riability in soils: high resolution assessment with electrical needle probe. J. Geotech. Geoenviron. Engng 130, No. 8, 843–850. https://doi.org/10.1061/(asce)1090-0241(2004)130:8(843)

Díaz-Rodríguez, J. A., Cruz, R. L. S., Dávila-Alcocer, V. M., Vallejo, E. and Girón, P. (1998). Physical, chemical, and m ineralogical properties of Mexico City sediments: a geotec hnical perspective. Can. Geotech. J. 35, No. 4, 600–610. ht tps://doi.org/10.1139/t98-026

Fernandez, A. L. and Santamarina, J. C. (2001). Effect of ceme ntation on the small-strain parameters of sands. Can. Geote ch. J. 38, No. 1, 191–199. https://doi.org/10.1139/t00-081

Lee, J. S. and Santamarina, J. C. (2005). Bender elements: perf ormance and signal interpretation. J. Geotech. Geoenviron. Engng 131, No. 9, 1063–1070. https://doi.org/10.1061/(asce)1090-0241(2005)131:9(1063)

Lee, J. S. and Santamarina, J. C. (2006). Discussion 'Measurin g shear wave velocity using bender elements' Eds. Leong, E. C., Yeo, S. H., Rahardjo, H. Geotech. Test. J. 29, No. 5, 1–5. https://doi.org/10.1520/gtj100382

Lee, C., Yun, T. S., Lee, J. S., Bahk, J. J. and Santamarina, J. C . (2011). Geotechnical characterization of marine sediment s in the Ulleung Basin, East Sea. Engng Geol. 117, No. 1–2, 151–158. https://doi.org/10.1016/j.enggeo.2010.10.014

Lee, I. M., Kim, J. S., Yoon, H. K. and Lee, J. S. (2014). Evalu ation of compressive strength and stiffness of grouted soils by using elastic waves. Scientific World J. 2014, article I D 215804. https://doi.org/10.1155/2014/215804

Lee, J. S., Lee, J. Y., Kim, Y. M. and Lee, C. (2013). Stress-de pendent and strength properties of gas hydrate-bearing mar ine sediments from the Ulleung Basin, East Sea, Korea. M

ar. Petrol. Geol. 47, 66–76. https://doi.org/10.1016/j.marpetgeo.2013.04.006
Losic, D., Pillar, R. J., Dilger, T., Mitchell, J. G. and Voelcker, N. H. (2007). Atomic force microscopy (AFM) characterisation of the porous silica nanostructure of two centric diatoms. J. Porous Mater. 14, No. 1, 61–69. https://doi.org/10.1007/s10934-006-9009-y
Hong, Z., Tateishi, Y. and Han, J. (2006). Experimental study of macro- and micro-behavior of natural diatomite. J. Geotech. Geoenviron. Engng 132, No. 5, 603–610. https://doi.org/10.1061/(asce)1090-0241(2006)132:5(603)
Owen, R. B., Renaut, R. W. and Stamatakis, M. G. (2010). Diatomaceous sedimentation in late neogene lacustrine basins of western Macedonia, Greece. J. Paleolimnol. 44, No. 1, 343–359. https://doi.org/10.1007/s10933-010-9409-5
Tanaka, H. and Locat, J. (1999). A microstructural investigation of Osaka Bay clay: the impact of microfossils on its mechanical behaviour. Can. Geotech. J. 36, No. 3, 493–508. https://doi.org/10.1139/t99-009
Tréguer, P., Nelson, D. M., Van Bennekorn, A. J., DeMaster, D. J., Leynaert, A. and Quéguiner, B. (1995). The silica balance in the world ocean: a reestimate. Science 268, No. 5209, 375–379. https://doi.org/10.1126/science.268.5209.375
Salgado, R., Bandini, P. and Karim, A. (2000). Shear strength and stiffness of silty sand. J. Geotech. Geoenviron. Engng 126, No. 5, 451–462. https://doi.org/10.1061/(asce)1090-0241(2000)126:5(451)
Santamarina, J. C., Klein, A. and Fam, M. A. (2001). Soils and waves: particulate materials behavior, characterization and process monitoring, vol. 1. New York, NY, USA: John Wiley and Sons. https://doi.org/10.1007/bf02987719
Shiwakoti, D. R., Tanaka, H., Tanaka, M. and Locat, J. (2002). Influences of diatom microfossils on engineering properties of soils. Soils Found. 42, No. 3, 1–17. https://doi.org/10.3208/sandf.42.3_1
Wiemer, G., Dziadek, R. and Kopf, A. (2017). The enigmatic consolidation of diatomaceous sediment. Mar. Geol. 385, 173–184. https://doi.org/10.1016/j.margeo.2017.01.006
Yun, T. S. and Santamarina, J. C. (2005). Decementation, softening, and collapse: changes in small-strain shear stiffness in k0 loading. J. Geotech. Geoenviron. Engng 131, No. 3, 350–358. https://doi.org/10.1061/(asce)1090-0241(2005)131:3(350)
Zhang, D., Wang, Y., Zhang, W., Pan, J. and Cai, J. (2011). Enlargement of diatom frustules pores by hydrofluoric acid etching at room temperature. J. Mater. Sci. 46, No. 17, 5665–5671. https://doi.org/10.1007/s10853-011-5517-5